Electronic Supplementary Information

Durable and efficient urea electrosynthesis through carbon dioxide and nitrate over the defect-rich In$_2$O$_3$ nanotube

Hongjun Fang[a], Chen-Han Kuo[a], Hongsheng Yang[a], Ze Wang[a], Xinzhen Feng[a],

Weijie Ji[a] [*], Chak-Tong Au[b]

[a] Key Laboratory of Mesoscopic Chemistry, MOE, School of Chemistry and Chemical

Engineering, Nanjing University, Nanjing 210023, China

[b] Department of Chemistry, Hong Kong Baptist University, Hong Kong

*Corresponding author.

E-mail address: jiwj@nju.edu.cn

Materials

Potassium nitrate (KNO_3), potassium nitrate-^{15}N ($K^{15}NO_3$), potassium nitrite (KNO_2), ammonium chloride (NH_4Cl), sodium citrate ($C6H_5O_7Na_3$) are purchased from Sinopharm Chemical Reagent Co. Ltd., hydrazine monohydrate ($N_2H_4 \cdot H_2O$), indium nitrate tetrahydrate ($In(NO_3)_3 \cdot 4H_2O$), terephthalic acid (H_2BDC), N, N-dimethylformamide (C_3H_7NO), diacetylmonoxime ($C_4H_7NO_2$), thiosemicarbazide (CH_5N_3S), iron trichloride ($FeCl_3$), sodium nitroferricyanide dihydrate ($C_5FeN_6Na_2O \cdot 2H_2O$), sodium hypochlorite solution ($NaClO$), N-(1-naphthyl) ethylenediamine dihydrochloride ($C_{12}H_{14}N_2$), sulfonamide ($H_4N_2O_2S$), hosphoric acid (H_3PO_4), dimethyl sulfoxide-d_6 (d_6-DMSO) are purchased from Aladdin. Carbon paper (CP) was purchased from Suzhou Sinero Technology Co. Ltd. All reagents are analytical grade without further purification.

Electrochemical measurements

The electrochemical measurements were conducted on a CHI 660E electrochemical workstation with a three-electrode configuration, of which platinum sheet, Ag/AgCl, catalyst coated carbon paper were used as the counter electrode, reference electrode and working electrode, respectively. For preparation of working electrode, 5 mg of as-prepared catalyst was dispersed into a mixture containing 970 μL of ethanol and 30 μL of 5 wt% nafion solution, followed by ultrasonic treatment to form a homogeneous catalyst ink. Then, 20 μL of the catalyst ink was coated onto carbon paper (CP, 1×0.5 cm^{-2}, catalyst loading of 0.2 mg cm^{-2}) and dried at 80 °C. Liner sweep

voltammetry (LSV) measurements were measured in CO_2-saturated or Ar-saturated electrolyte containing $0.1M\ NO_3^-$ at a scan rate of 10 mV s^{-1}. Cyclic voltammetry (CV) was performed in CO_2-saturated electrolyte containing $0.1M\ NO_3^-$ within a potential range from 0.28 V to 0.38 V vs. RHE. Electrochemical impedance spectroscopy (EIS) was performed at the frequency range of 10^6 to 10^{-2} Hz and an amplitude of 5 mV. Mott-Schottky curve was measured at the fixed frequency of 1000 Hz with an amplitude of 5 mV.

Characterization method

Powder X-ray diffraction (XRD) was performed on a Philips X'Pert MPD Pro X-ray diffractometer with Cu Kα radiation. Scanning electron microscopy (SEM) was recorded on a Hitachi S-4800 microscope. X-ray photoelectron spectroscopy (XPS) was determined by a PHI5000 Versa Probe spectrometer with Al Kα irradiation. The high-resolution transmission electron microscopy (HR-TEM) was carried out on the TECNAI G2 F30. Element mapping was performed on an energy dispersive spectrometer (EDAX GENESIS). In situ attenuated total reflection Fourier Transform infrared spectroscopy (ATR-FTIR) was carried out on the Perkin Elmer 3 spectrometer. A thin gold film is chemically deposited on the surface of a silicon crystal, then the catalyst ink (100 μl, 10 mg /mL) was dropped onto the gold film, and the whole device was employed as working electrode. The counter electrode and reference electrode were platinum foil and Ag/AgCl, and the electrolyte was $0.1M\ KNO_3$, which was purged with CO_2 during the electrocatalytic processes. After chronoamperometry

3

operation in the potential range of -0.42 V ~ -0.72 V vs. RHE, we collected the corresponding ATR-FTIR spectra.

Isotopic labeling experiment

The isotope-labelled experiments were carried out using $K^{15}NO_3$ as a N source and CO_2 as a feeding gas. After electrolysis at -0.52 V for 1 h, the cathodic liquid was frozen and dried to obtain the electrolyte powder, followed by introduction of d_6-DMSO solution (1 mL). After ultrasonic dispersion, the resulting mixture was centrifuged and the supernatant was extracted for ^1H nuclear magnetic resonance (NMR) measurement.

DFT calculation

All spin-polarized density-functional theory (DFT) computations were performed using the Vienna ab initio simulation package (VASP) based on the projector augmented wave (PAW) method.[1,2] To study the mechanistic chemistry of surface reactions, the surface was modelled with a slab model. A large vacuum region of 15 Å was used to ensure the periodic images were well separated. During the geometry optimizations, the bottom atoms were fixed at the bulk position when the surface properties were calculated. The Brillouin-zone integrations were conducted using Monkhorst-Pack grids of special points with a separation of 0.06 Å^{-1}.[14] The convergence criterion for the electronic self-consistent loop was set to 10^{-5} eV. The atomic structures were optimized until the residual forces were below 0.03 eV Å^{-1}.

The adsorption energy (E_{ads}) of the adsorbent on the substrate was calculated by

the equation (1):

$$E_{ads} = E_{substrate+adsorbate} - E_{substrate} - E_{adsorbate} \ (1)$$

Where $E_{substrate+adsorbate}$ refers to the total energy of catalyst surface with the adsorbate, $E_{substrate}$ and $E_{adsorbate}$ are the total energy of catalyst surface and the adsorbates, respectively.

The Gibbs free energy change (ΔG) of each step was obtained by the equation (2):

$$\Delta G = \Delta E + \Delta E_{ZPE} - T\Delta S \ (2)$$

Where the ΔE denotes the adsorption energy, ΔE_{ZPE} and ΔS are the changes of zero-point energy and entropy, and the temperature T is set to 300 K.

Determination of products

Determination of urea: The generated urea was quantified by diacetyl monoxime method.[10] Briefly, electrolyte of 1 mL was drawn from the cathode chamber, followed by addition of 2 mL acidic iron solution (30 mL of concentration sulfuric acid and 10 mg $FeCl_3$ were dissolved in 60 mL H_2O) and DAMO-TSC solution of 1 mL (diacetylmonoxime of 500 mg and thiosemicarbazide of 100 mg were dissolved into 100 mL of H_2O). The resulting suspension was then heated to 100 °C and maintained for 20 min. After that, the absorbance of the solution was measured by means of a UV-vis spectrophotometer at a wavelength of 525 nm. The concentration-absorbance calibration curves were made by using a set of standard urea solutions (Fig. S1), which contained the electrolyte of the same concentration used in electrocatalytic experiments.

Determination of NH$_3$: The produced NH$_3$ was measured by the indophenol blue method. Typically, 2 mL of catholyte, 2 mL of NaOH solution (1 M, containing 5% salicylic acid and 5% sodium citrate), 1 mL of NaClO solution (0.05M), and 0.2 mL of 1% C$_5$FeN$_6$Na$_2$O·2H$_2$O were mixed together. After the dark treatment for 2 h, the concentration of NH$_3$ was measured by UV-vis spectrophotometer at a wavelength of 655 nm. The concentration-absorbance curves were calibrated by using standard ammonium chloride solutions (Fig. S2), which contained the same concentration of electrolytes that were used in electrocatalytic experiments.

Determination of NO$_2^-$: The concentration of NO$_2^-$ was determined by the Griess method. Briefly, 0.1 g of N-(1-naphthol) ethylenediamine dihydrochloride, 1.0 g of sulfonamide, and 2.94 mL of phosphoric acid were mixed in 50 mL deionized water to prepare the Griess reagent. Subsequently, 1 mL of cathodic electrolyte, 1 mL of Griess reagent and 2 mL of deionized water were mixed together. After the dark treatment for 15 min, the solution absorbance was measured by UV-vis spectrophotometer at a wavelength of 540 nm. The concentration-absorbance curves were calibrated by using standard potassium nitrite solutions (Fig. S3), which contained the same concentration of electrolytes that were used in electrocatalytic experiments.

Determination of N$_2$H$_4$: The concentration of N$_2$H$_4$ was determined by the Watt-Chrisp method. To obtain the Watt-Chrisp reagent, 5.99 g of para-(dimethylamino) benzaldehyde, hydrochloric acid (30 mL), and ethanol (300 mL) were mixed together. Next, 2 mL of cathodic electrolyte was added to 5 mL of the Watt-Chrisp reagent at room temperature. After the dark treatment for 30 min, the solution absorbance was

measured by UV-vis spectrophotometer at a wavelength of 457 nm. The concentration-absorbance curves were calibrated by using standard hydrazine monohydrate solutions (Fig. S4), which contained the same concentration of electrolytes that were used in electrocatalytic experiments.

Determination of gaseous products: The gaseous products of H_2 and CO were analyzed by online gas chromatography (GC126N) with a thermal conductivity detector (TCD) and flame ionization detector (FID), respectively.

The faradaic efficiency (FE) of these generated products is calculated by the following equations:

$$\text{Urea production rate} = (C_{urea} \times V) / (t \times m)$$

$$FE_{urea} = (16 \times F \times C_{urea} \times V) / (60.06 \times Q) \times 100\%$$

$$FE_{NH3} = (8 \times F \times C_{NH3} \times V) / (17 \times Q) \times 100\%$$

$$FE_{NO2-} = (2 \times F \times C_{NO2-} \times V) / (46 \times Q) \times 100\%$$

$$FE_{CO} = (2 \times F \times n_1) / Q$$

$$FE_{H2} = (2 \times F \times n_2) / Q$$

where F is Faraday constant (96485 C mol^{-1}), Q is the quantity charge (C), C is the measured concentration of product, V is the electrolyte volume (40 mL), n_1 and n_2 are the molar amount of CO and H_2, respectively.
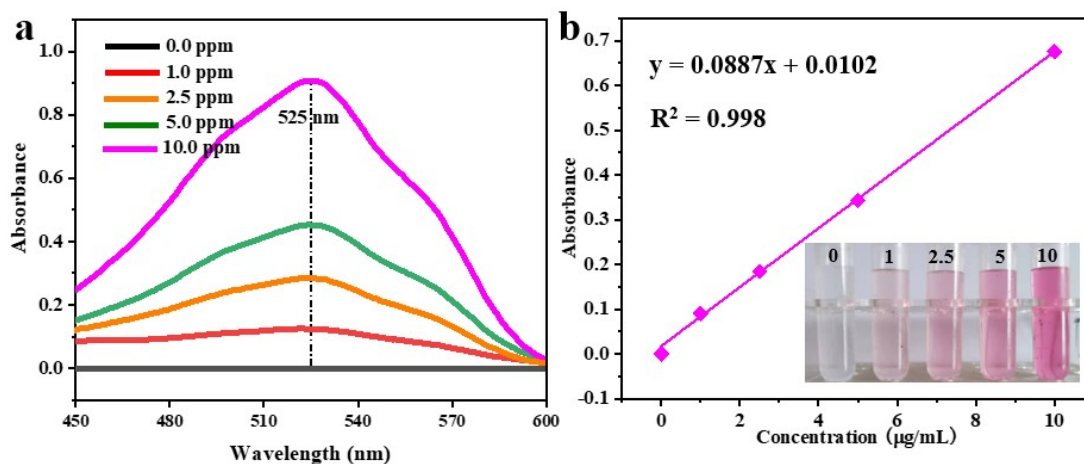
Fig. S1. (a) UV-vis absorption spectra, (b) corresponding calibration curve used for calculation of urea concentration
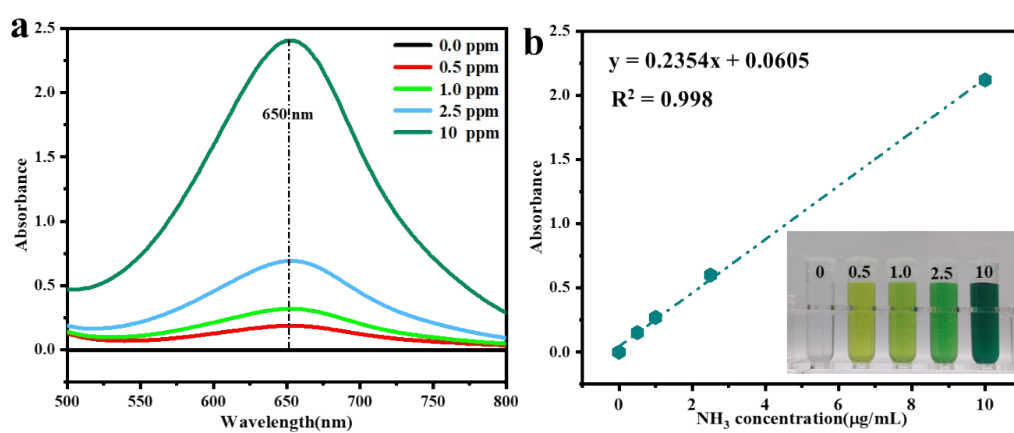

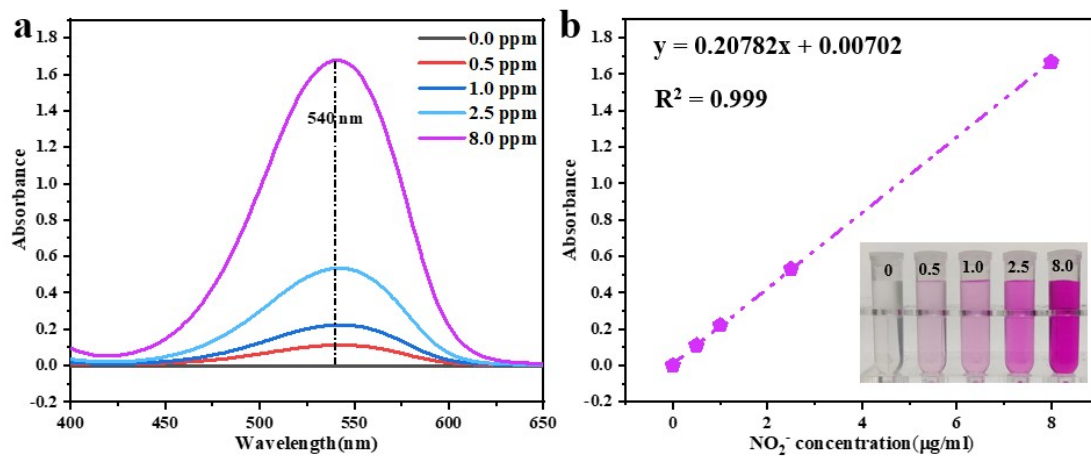**Fig. S2.** (a) UV-vis absorption spectra, (b) corresponding calibration curve used for calculation of NH_3 concentration.

Fig. S3. (a) UV-vis absorption spectra, (b) corresponding calibration curve used for calculation of NO_2^- concentration.
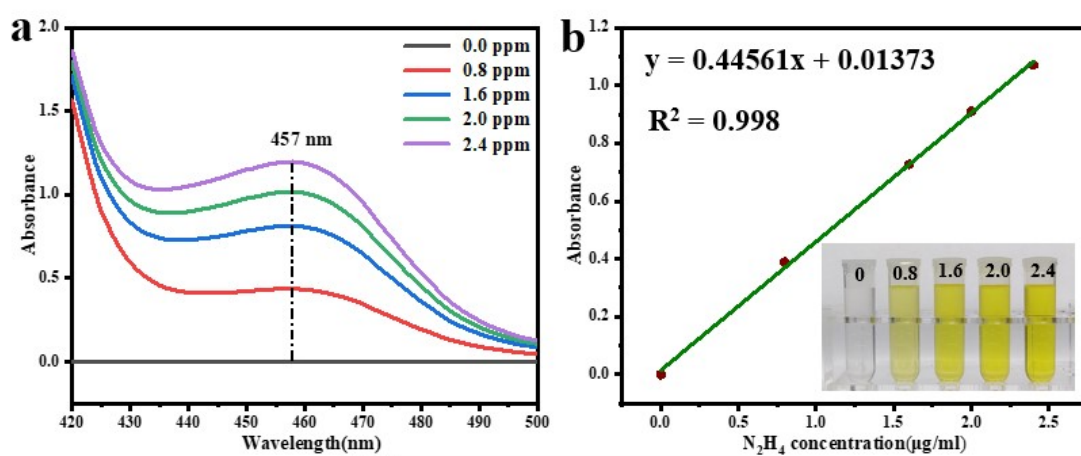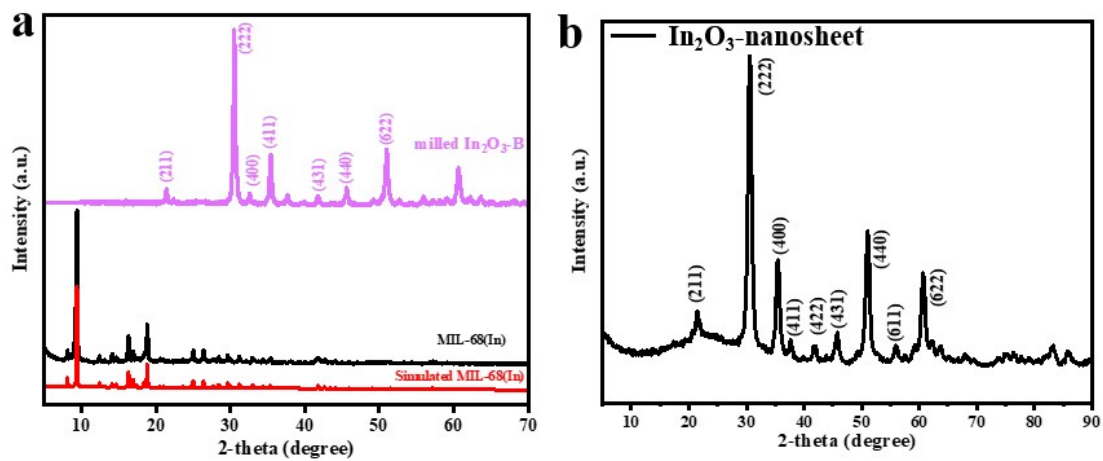

Fig. S4. (a) UV-vis absorption spectra, (b) corresponding calibration curve used for calculation of N_2H_4 concentration.

Fig. S5. XRD patterns of (a) MIL-68(In), milled In_2O_3-B and (b) In_2O_3 nanosheet.
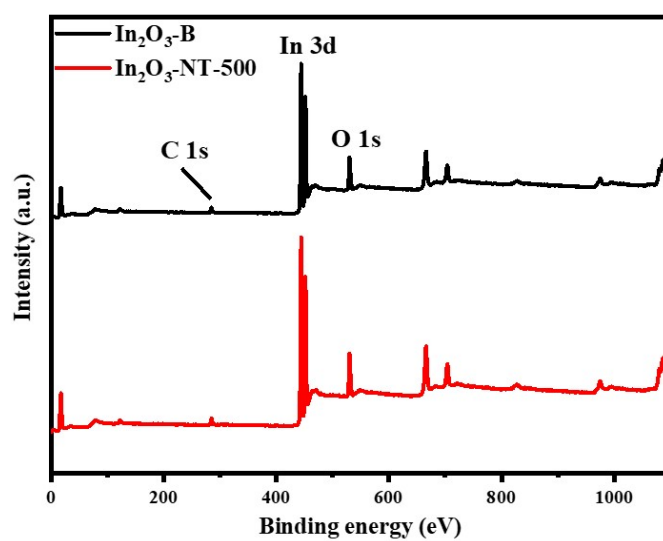
Fig. S6. XPS survey spectra of In_2O_3-NT-500 and In_2O_3-B.
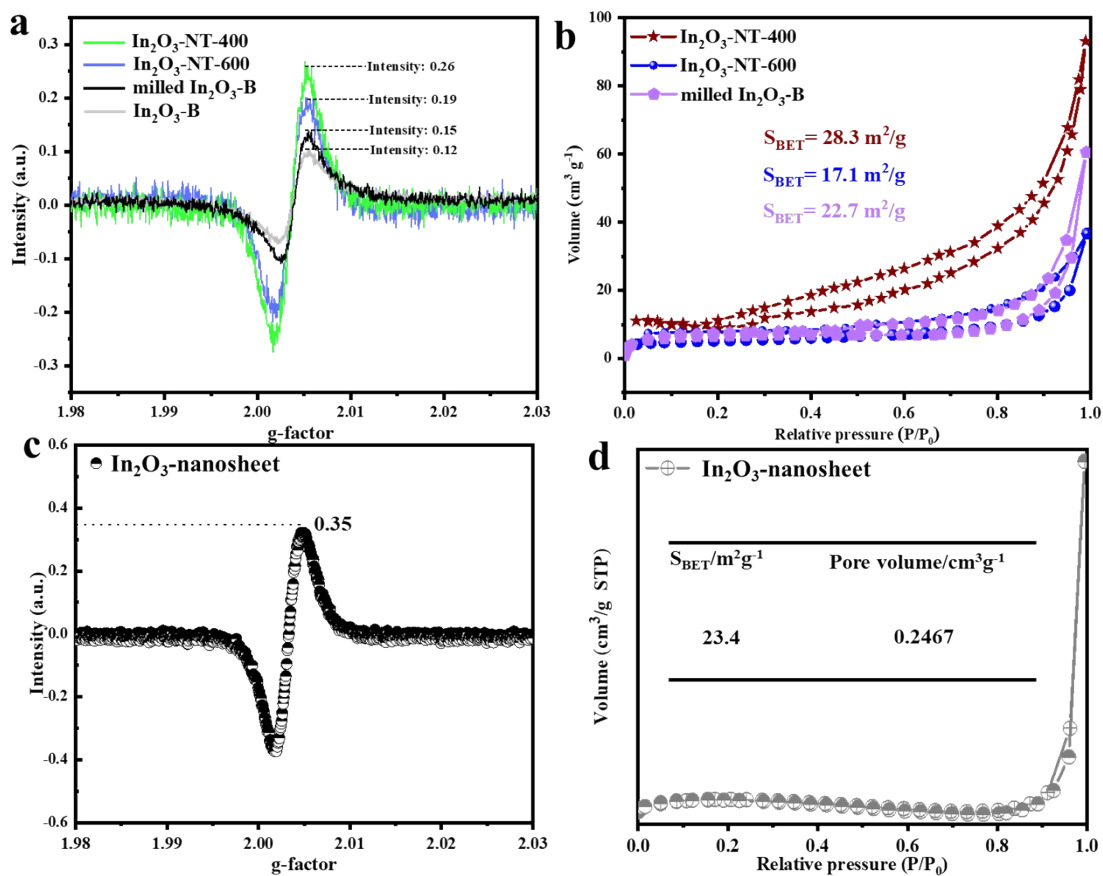
Fig. S7. (a-c) the EPR spectra of In_2O_3-NT-400, In_2O_3-NT-600, In_2O_3-B, milled In_2O_3-B and In_2O_3 nanosheet; (b-d) N_2 adsorption-desorption isotherms and the corresponding S_{BET} of In_2O_3-NT-400, In_2O_3-NT-600, milled In_2O_3-B and In_2O_3 nanosheet.
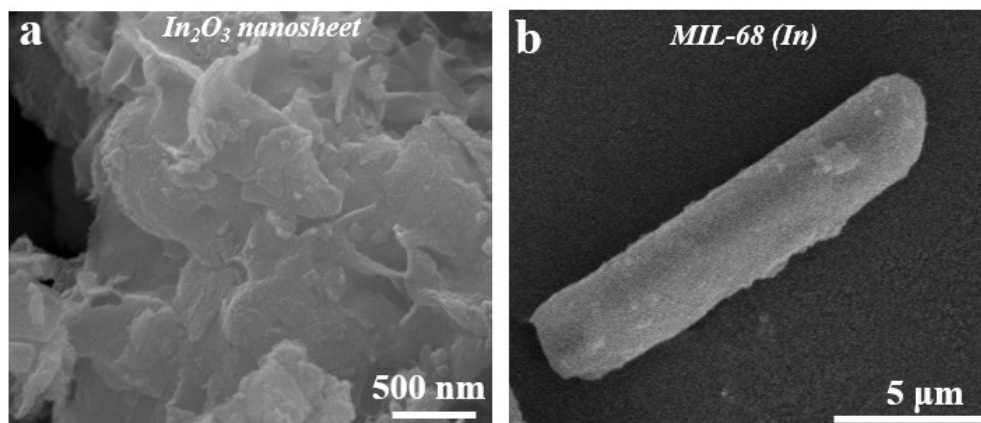
Fig. S8. SEM images of (a) In_2O_3 nanosheet and (b) MIL-68(In).
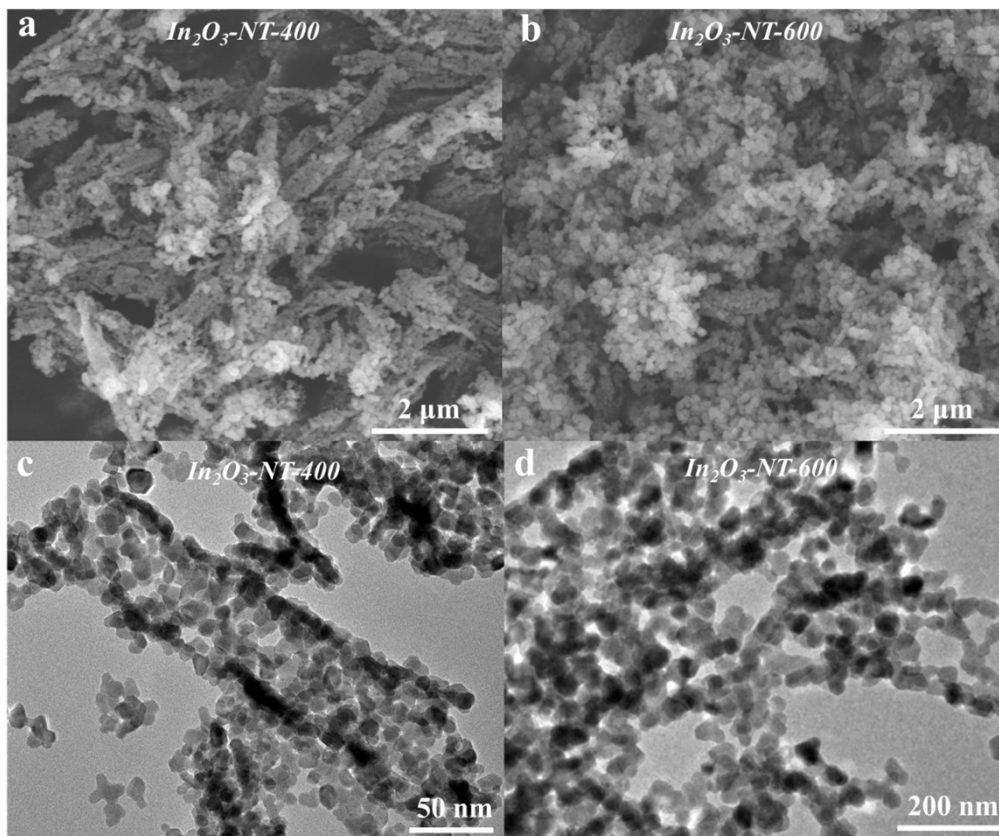
Fig. S9. SEM and TEM images of (a-c) In$_2$O$_3$-NT-400 and (b-d) In$_2$O$_3$-NT-600.
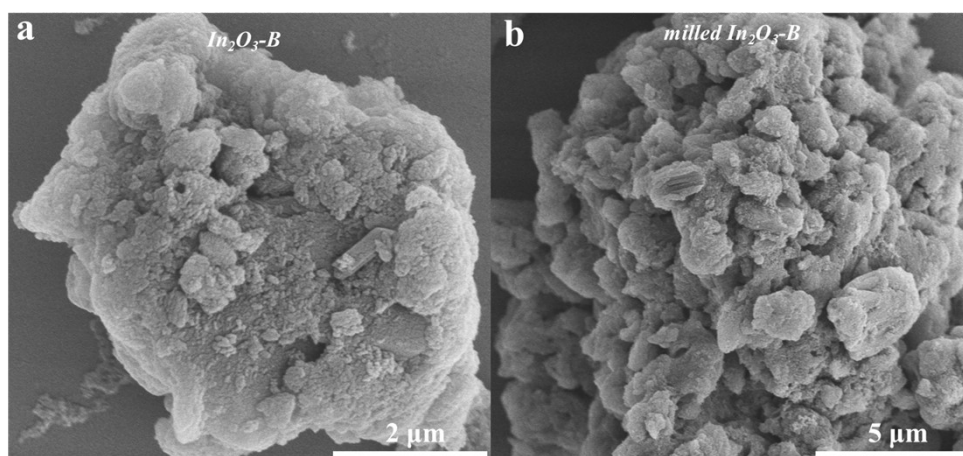

Fig. S10. SEM image of (a) In$_2$O$_3$-B and (b) milled In$_2$O$_3$-B after ball-milling.
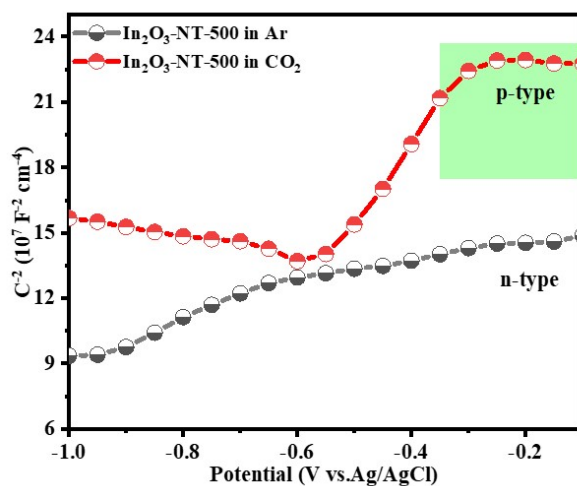
Fig. S11. Mott-Schottky curves of In_2O_3-NT-500 electrode in Ar- and CO_2-saturated
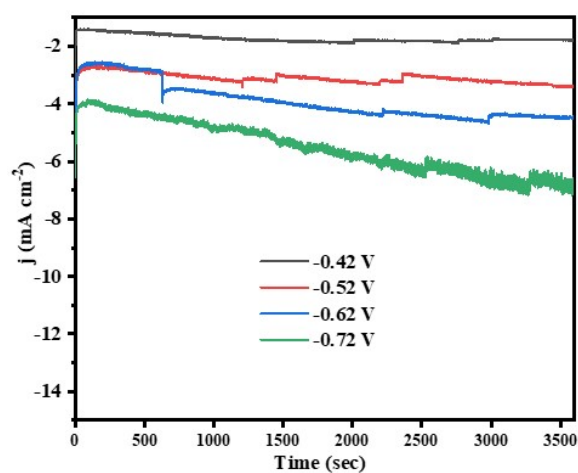
electrolyte.

Fig. S12. Chrono-amperometry curves of In_2O_3-NT-500 electrode in each given
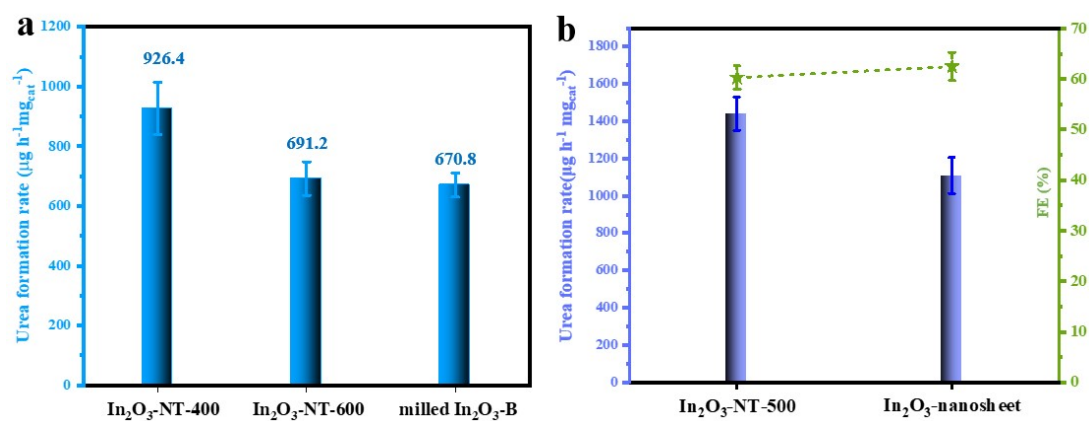
potential.

Fig. S13. (a) urea formation rates of In_2O_3-NT-400, In_2O_3-NT-600 and milled In_2O_3-B electrode, (b) urea formation rates and FEs of In_2O_3-NT-500 and In_2O_3 nanosheet.

S_{BET} and relative Vo content of catalysts

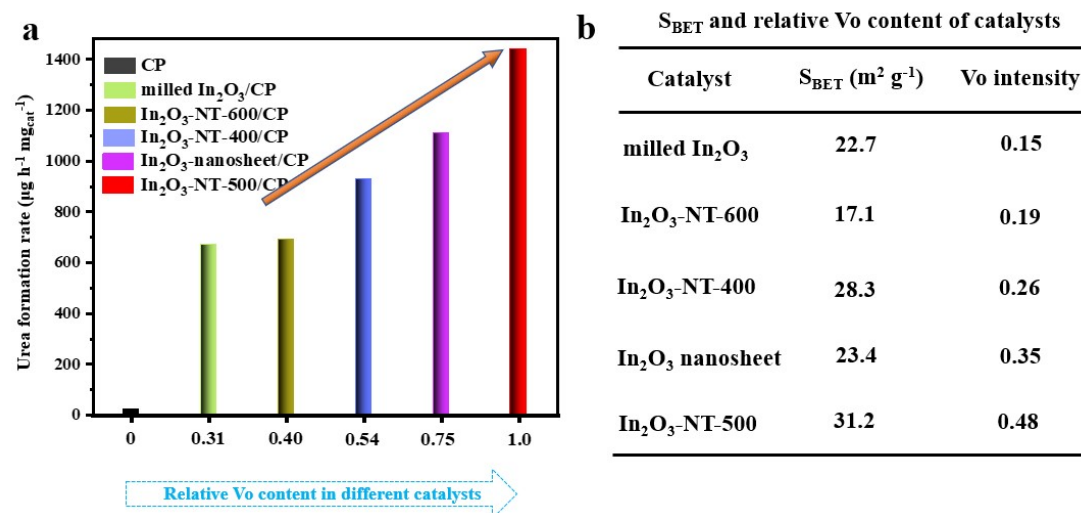| Catalyst	S_{BET} (m^2 g^{-1})	Vo intensity
milled In_2O_3	22.7	0.15
In_2O_3-NT-600	17.1	0.19
In_2O_3-NT-400	28.3	0.26
In_2O_3 nanosheet	23.4	0.35
In_2O_3-NT-500	31.2	0.48

Fig. S14. (a) the relationship between Vo ratio and urea production rate (herein Vo ratio was calculated according to the signal intensity of the EPR, using In_2O_3-NT-500 as the reference); (b) the S_{BET} and relative Vo content of catalysts.

a — FE (%) vs Potential (V vs. RHE): Urea, NO_2^-, NH_3, H_2

b — Absorbance vs Wavelength (nm): −0.42V, −0.52V, −0.62V, −0.72V

c — Ag/AgCl; Pt sheet (anode); Working electrode (cathode)

Cathode: $NO_3^- + 9H^+ + 8e^- \rightarrow NH_4^+ + 3H_2O$

$NO_2^- + 6H^+ + 6e^- \rightarrow NH_4^+ + H_2O$

Anode: $2Cl^- - 2e^- \rightarrow Cl_2\ (g)$

$Cl_2\ (g) + H_2O \rightarrow ClO^- + Cl^- + 2H^+$

$NO_2^- + ClO^- \rightarrow NO_3^- + Cl^-$ (minor)

$2NH_4^+ + 3ClO^- \rightarrow N_2\ (g) + 3Cl^- + 2H^+ + 3H_2O$ (major)

d — NO_2^- concentration ($\mu g\ mL^{-1}$) vs Time (min): Co-electrolysis of CO_2 and NO_3^- at −0.52V for 1h; Electro-chlorination at given potential for 2h; at −0.52V vs. RHE; at −0.62V vs. EHE; at −0.72V vs. RHE; at −0.82V vs. RHE
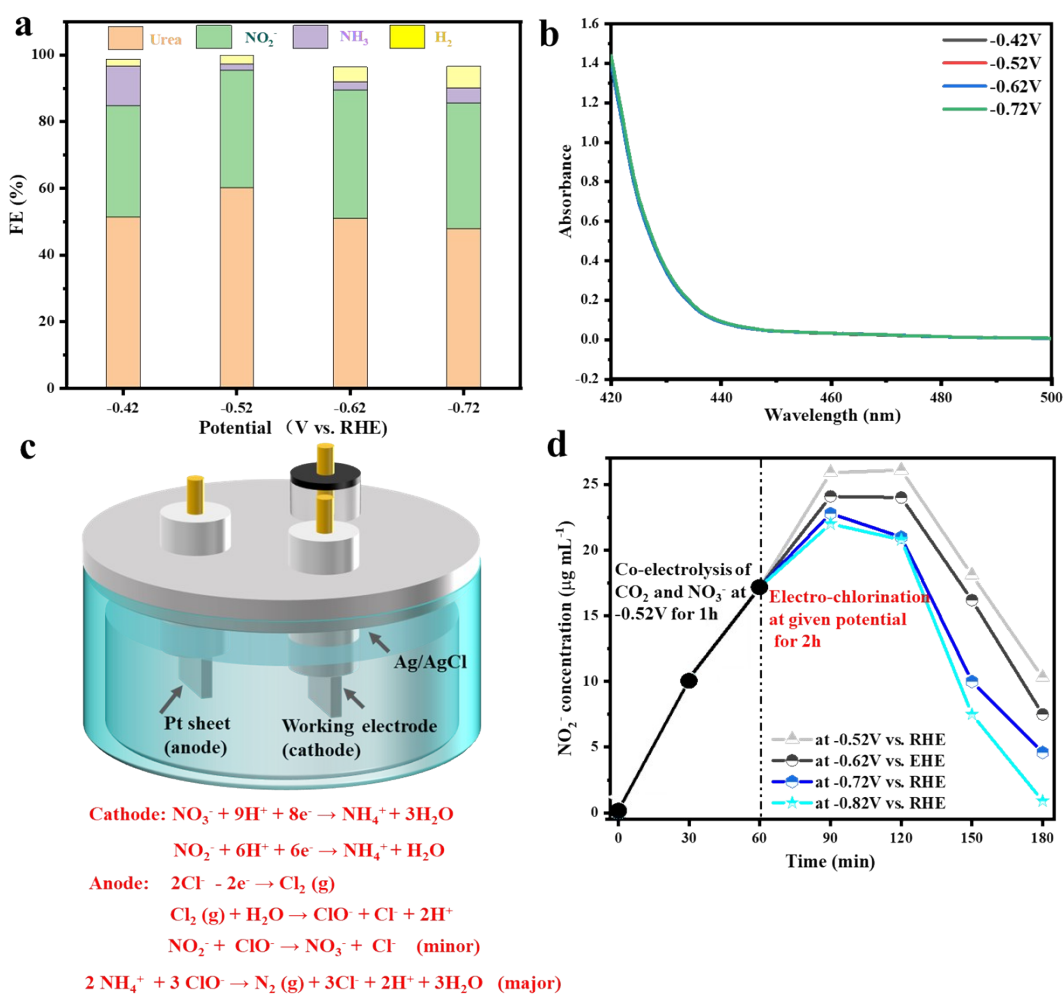
Fig. S15. (a) the relative FE of the generated products; (b) UV-vis absorption spectra of the electrolyte after electrocatalysis at different potentials using In_2O_3-NT-500 as catalyst; (c) the electrochemical configuration used for electro-chlorination test (Condition: the electrolyte of 40 mL was obtained from the used electrolyte after co-reduction of CO_2/NO_3^- at -0.52 V for 1h on the In_2O_3-NT-500 electrode, and the working electrode was the second-hand In_2O_3-NT-500 electrode obtained from the urea electrosynthesis test, $[Cl^-] = 0.15$ M); (d) the concentration of NO_2^- during electrocatalytic reaction.
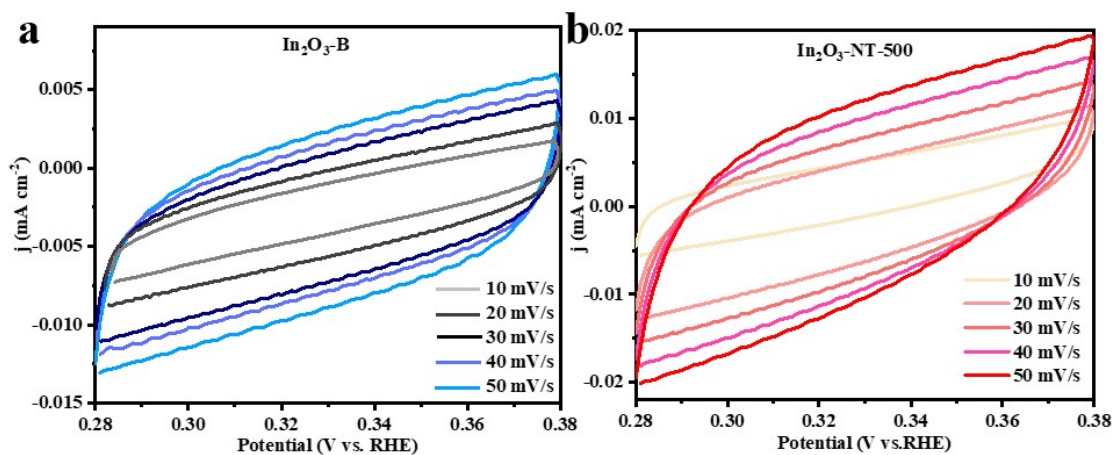
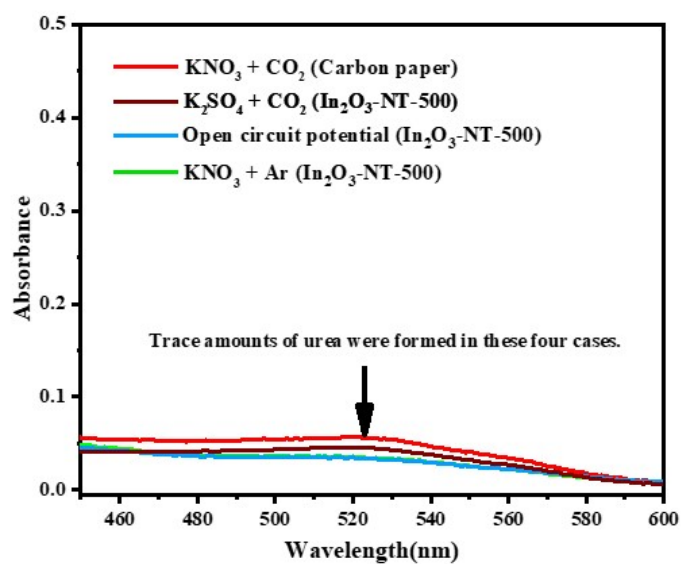**Fig. S16.** CV curves of (a) In$_2$O$_3$-B and (b) In$_2$O$_3$-NT-500 electrode at different scanning rates.

Fig. S17. UV-vis adsorption spectra of In$_2$O$_3$-NT-500 electrode after electrolysis at the specific conditions for 1h.
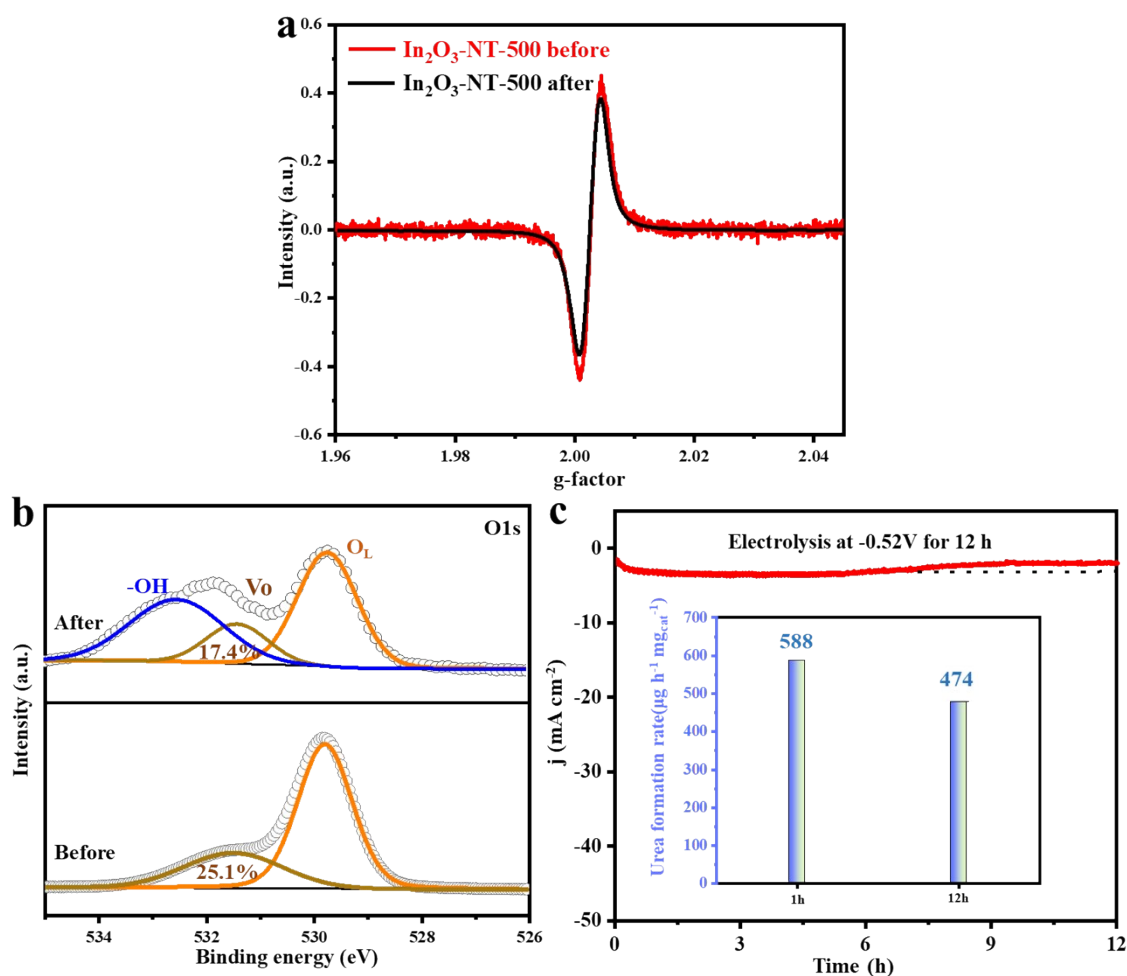
Fig. S18. (a) the EPR spectra of In_2O_3-NT-500 electrode before and after reaction; (b) O 1s XPS spectra of In_2O_3-B before and after electrocatalytic reaction, (c) chronoamperometric curves of In_2O_3-B electrode during 12-h reaction, and the inset is the related urea production rates at 1st cycle and 12th cycle.

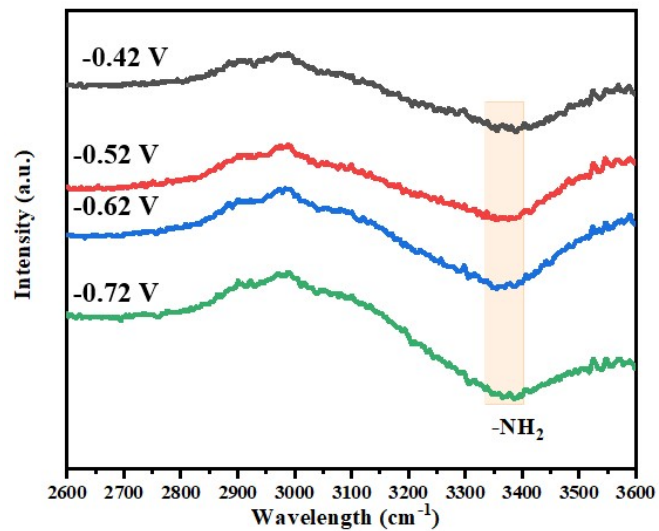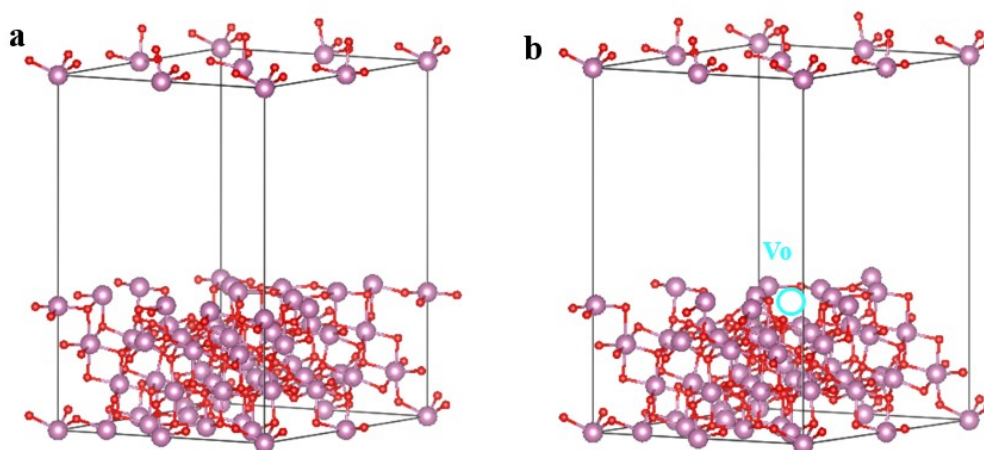**Fig. S19.** In situ ATR-FTIR spectra of In$_2$O$_3$-NT-500 electrode in the wavelength range of 2600 ~ 3600 cm^{-1}.

Fig. S20. The structural models of (a) Vo-deficient In$_2$O$_3$ (222) and (b) Vo-rich In$_2$O$_3$ (222) facet.
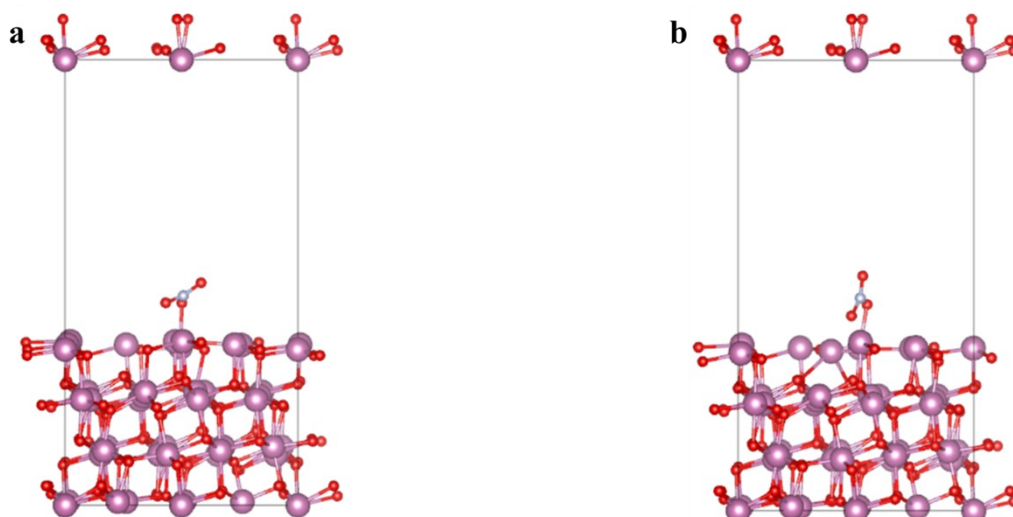
Fig. 21. The adsorption configuration of NO_3^- on (a) Vo-deficient In_2O_3 (222) and (b) Vo-rich In_2O_3 (222) facet.
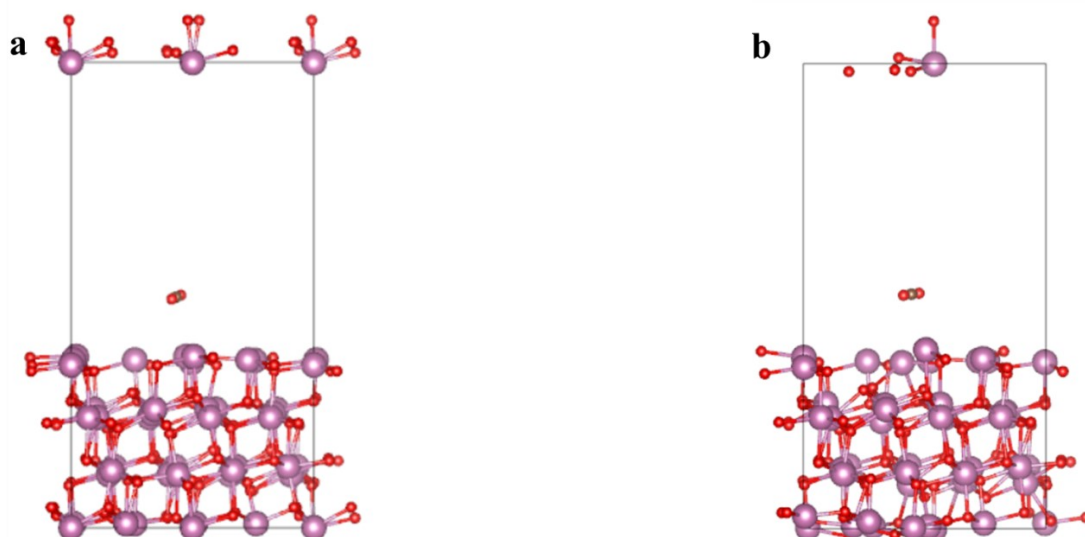

Fig. 22. The adsorption configuration of CO_2 on (a) Vo-deficient In_2O_3 (222) and (b) Vo-rich In_2O_3 (222) facet.
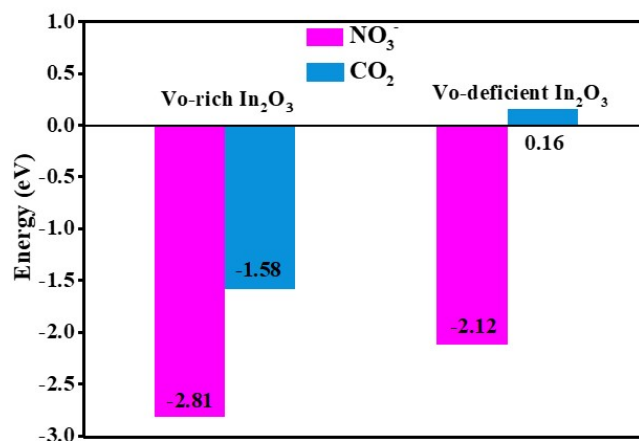
Fig. 23. The adsorption free energy of CO_2 and NO_3^- on the Vo-rich In_2O_3 (222) and Vo-deficient In_2O_3 (222) surface.
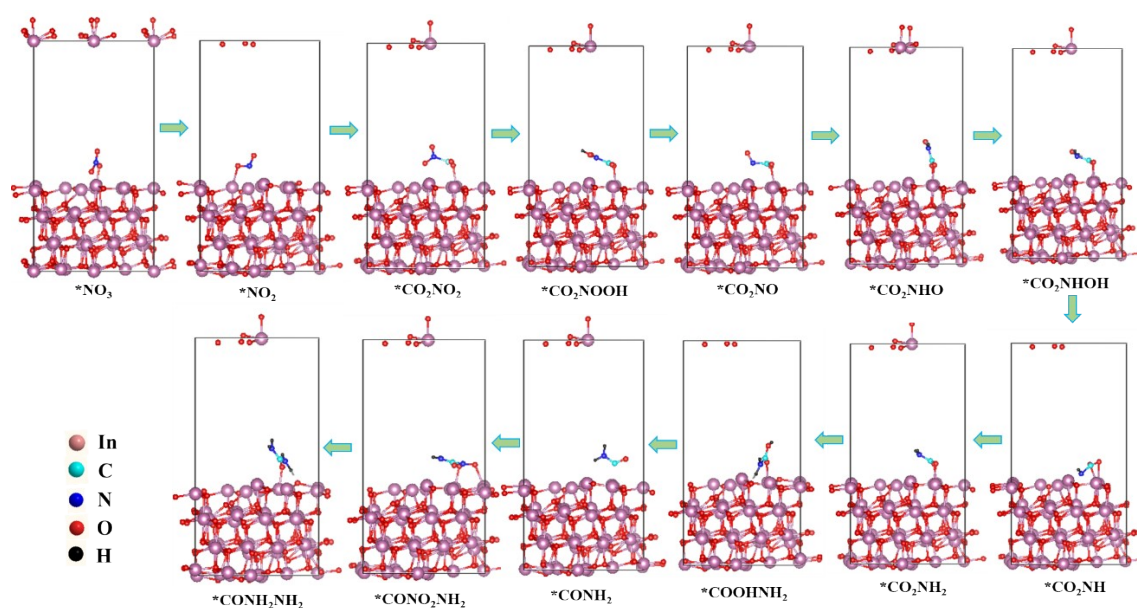

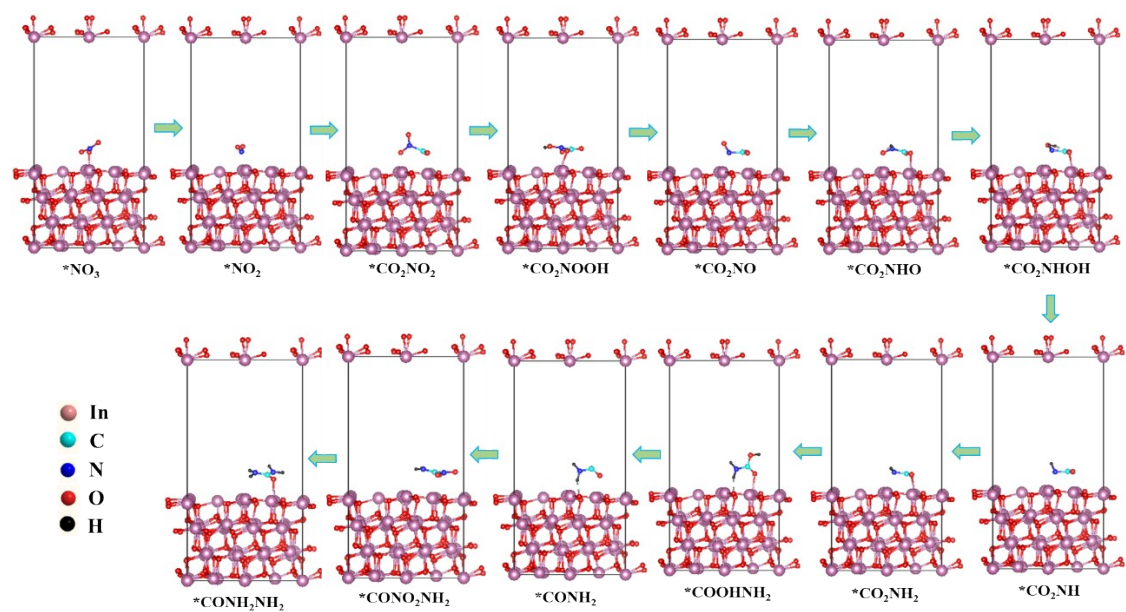**Fig. S24.** Structure diagrams of C-N coupling processes on Vo-rich In_2O_3 (222) surface.

Fig. S25. Structure diagrams of C-N coupling processes on Vo-deficient In_2O_3 (222) surface.

Table S1. The performance comparison of In_2O_3-NT-500 with other reported electrocatalysts for urea production.

Electrocatalyst	Electrolyte	Urea formation rate ($\mu g\ h^{-1}\ mg_{cat}^{-1}$)	Faradaic efficiency	Reference
In_2O_3-NT-500	0.1M NO_3^- and CO_2	1441.5	60.3% at -0.52V	This work
Fe-Ni catalyst	CO_2-saturated 0.1M $KHCO_3$ + 50 mM NO_3^-	1213.2	17.8% at -1.5 V	Nat. Commun. (Zhang et al., 2022)
CeO_2-Ov	CO_2-saturated 0.1M $KHCO_3$ + 50 mM NO_3^-	943.6	4.5% at -1.60V	J. Am. Chem. Soc. (Wei et al., 2022)
C/MoOx	0.1M NO_3^- and CO_2	1431	27.7% at -0.60V	Angew. Chem. Int. Ed. (Sun et al., 2023)
Fe@C-Fe_3O_4/CNTs	0.1M NO_3^- and CO_2	1341	16.5% at -0.65V	Angew. Chem. Int. Ed. (Geng et al., 2023)
AuPd nanoalloy	CO_2-saturated 75 mM $KHCO_3$ + 25 mMNO_3^-	204.2	15.6% at -0.40V	Appl. Catal. B Environ. (Wang et al., 2022)
F-CNT	0.1M NO_3^- and CO_2	381.9	18.0% at -0.65V	Appl. Catal. B Environ. (Liu et al., 2022)
$In(OH)_3$-S	0.1M NO_3^- and CO_2	533.1	54.3% at -0.60V	Nat. Sustain. (Lv et al., 2021)
InOOH-Ov	0.1M NO_3^- and CO_2	592.5	51.0% at -0.50V	ACS Nano (Lv et al., 2022)
$BiFeO_3$/$BiVO_4$	N_2 and CO_2-saturated 0.1 M $KHCO_3$	297.3	17.2% at -0.40V	Chem. Sci. (Yuan et al., 2021)
$BiVO_4$	N_2 and CO_2-saturated 0.1 M $KHCO_3$	354.9	12.5% at -0.40 V	Angew. Chem. Int. Ed. (Zhao et al., 2021)
$CuWO_4$	0.1M NO_3^- and CO_2	95.8	70.1% at -0.20V	Nat. Commun. (Yin et al., 2023)
Bi/In/C	CO_2-saturated 0.1M $KHCO_3$ + 0.1M NO_3^-	606.4	20.3% at -0.45V	Appl. Catal. B Environ. (Mao et al., 2024)
FeOOH@$BiVO_4$	0.1M NO_3^- and CO_2	828.8	11.5% at -0.80 V	J. Energy Chem. (Yin et al., 2023)

References

1. X. R. Zhang, X. R. Zhu, C. Chen, J. Y. Zheng, S. P. Jiang, S. Y. Wang, *Nat. Commun.*, 2022, 13, 5337.

2. X. X. Wei, X. J. Wen, Y. Y. Liu, C. Chen, J. Chen, H. Z. Lin, X. Z. Fu, S. Y. Wang, *J. Am. Chem. Soc.*, 2022, 144, 11530-11535.

3. M. M. Sun, G. Z. Wu, J. D. Jiang, Y. D. Yang, A. J. Du, L. Dai, X. Mao, Q. Qin, *Angew. Chem. Int. Ed.*, 2023, 62, e202301957.

4. J. Geng, S. Ji, M. Jin, C. Zhang, M. Xu, G. Wang, C. Liang, H. Zhang, *Angew. Chem. Int. Ed.*, 2023, 62, e202210958.

5. H. Wang, Y. Jiang, S. J. Li, W. Luo, W. Shen, R. X. He, M. Li, *Appl. Catal. B Environ.*, 2022, 318, 121819.

6. X. Liu, P.V. Kumar, Q. Chen, L. Zhao, F. Ye, X. Ma, D. Liu, X. Chen, L. Dai, C. Hu, *Appl. Catal. B Environ.*, 2022, 316, 121618.

7. C. D. Lv, C. Lee, L. Zhong, H. Liu, J. Liu, L. Yang, C. Yan, W. Yu, H.H. Hng, Z. Qi, L. Song, S. Li, K.P. Loh, Q. Yan, G. Yu, *ACS Nano*, 2022, 16, 8213-8222.

8. C. D. Lv, L. X. Zhong, Z. W. Fang, S. Z. Li, Q. Y. Yan, G. H. Yu, *Nat. Sustain.*, 2021, 4, 868-876.

9. M.L. Yuan, J.W. Chen, Y.L. Bai, Z.J. Liu, J.X. Zhang, T.K. Zhao, Q. Wang, S.W. Li, H. Y. He, G.J. Zhang, *Angew. Chem. Int. Ed*., 2021, 19, 11005-11013.

10. M.L. Yuan, J.W. Chen, Y.L. Bai, Z.J. Liu, J.X. Zhang, T.K. Zhao, Q.N. Shi, S.W. Li, X. Wang, G.J. Zhang, *Chem. Sci.*, 2021, 12, 6048-6058.

11. Y. L. Zhao, Y. X. Ding, W. L. Li, C. Liu, L. C. Sun, F. S. Li, *Nat. Commun.*, 2023, 14, 4491.

12. Y. N. Mao, Y. jiang, Q. Gou, S. M. Lv, Z. Y. Song, L. R. Zheng, W. Su, R. X. He, *Appl. Catal. B Environ.*, 2024, 340, 123189.

13. H. Q. Yin, Z. S. Sun, Q. P. Zhao, L. L. Yang, Z. M. Zhang, *J. Energy Chem.*, 2023, 84, 385-393.

14. D. J. Chadi. Special points for Brillouin-zone integrations. *Phys. Rev. B*, 1977, 16, 1746-1747.